SANDIA REPORT

SAND89—2090 • UC—404
Unlimited Release
Printed October 1989

Si Deposition Rates in a Two-Dimensional CVD Reactor and Comparisons With Model Calculations

William G. Breiland, Michael E. Coltrin

Prepared by
Sandia National Laboratories
Albuquerque, New Mexico 87185 and Livermore, California 94550
for the United States Department of Energy
under Contract DE-AC04-76DP00789

Issued by Sandia National Laboratories, operated for the United States Department of Energy by Sandia Corporation.

Available to DOE and DOE contractors from
Office of Scientific and Technical Information
PO Box 62
Oak Ridge, TN 37831

Prices available from (615) 576-8401, FTS 626-8401

Available to the public from
National Technical Information Service
US Department of Commerce
5285 Port Royal Rd
Springfield, VA 22161

NTIS price codes
Printed copy: A03
Microfiche copy: A01

Distribution
Category UC-404

SAND--89-2090

DE90 005003

SAND89-2090
Unlimited Release
Printed October 1989

Si Deposition Rates in a Two-Dimensional CVD Reactor and Comparisons with Model Calculations

William G. Breiland and Michael E. Coltrin

Sandia National Laboratories

Albuquerque, NM 87185

Abstract

Deposition rates are presented for silicon from silane in a helium carrier gas using a tubular CVD reactor with a two-dimensional flow geometry. Measured surface-temperature profiles, inlet gas velocities, total pressures, and silane/helium concentrations are reported, providing exact boundary conditions that can be used in a two-dimensional numerical CVD model. Comparisons are made between this data and two variations of a model by Coltrin, Kee, and Miller in which different empirical expressions for the silane and disilane reactive sticking coefficient are used.

CONTENTS

Introduction

In the last ten years there has been considerable effort to develop numerical models of the chemical vapor deposition (CVD) process [1,2]. The treatment of fluid mechanics in these models spans a wide range of sophistication and detail of treatment. Models have been developed to describe steady and transient flows in two-dimensional channels [3-14], three-dimensional channels [15-17], low-pressure CVD (LPCVD) reactors [18-23], rotating-disk reactors [24-32], impinging-jet reactors [33-35], stagnation-point flow reactors [36-40], and commercial "barrel" reactors [41-47]. The treatment of chemical reactions in recent models covers just as wide a range. Many models contain no chemistry at all, calculating just the temperature and velocity fields [4,7,25]. Diffusion-limited growth can be estimated with this type of model using the analogy between heat and mass transport [26,27,37]. One treatment of chemistry assumes that chemical equilibrium is established at the deposition surface [3,31,48,49]. Some models include the concentration of a single reactant species, assuming unit reaction probability upon collision with the surface (or, equivalently, zero concentration at the surface) [8-15,43-45]. In these cases, deposition rates are calculated from the resulting concentration gradient. Another level of detail is obtained in some models that include 1 or 2 gas-phase reactions, and calculate species concentrations for the reactant as well as 1 or 2 intermediate species [16-21,32-34,39-42]. At the most detailed level of treating chemistry are models that include dozens of gas-phase and surface reactions and 10 or more gas-phase and surface chemical species concentrations [5,6,24,50-52].

In general, there is a trade-off between treatment of complex flow fields and detailed chemistry. Treating three-dimensional or transient flows or complex reactor geometries is so computationally demanding that chemical detail must be greatly simplified or omitted altogether. On the other hand, fluid mechanical complexity can be greatly

minimized by considering reactor configurations in which a similarity transformation converts the problem to one-dimensional flow, allowing treatment of dozens [24,50] to hundreds of reactions [51].

A model that lies between these two extremes is that of Coltrin, Kee, and Miller (CKM) [5,6], who calculated the coupled gas-phase fluid flow and chemical kinetics in the deposition of Si from SiH_4 in a two-dimensional channel reactor. This model calculates gas-phase temperature and velocity fields, concentration fields for 17 chemical species, and deposition rate along the channel length as a function of parameters such as flow rate, susceptor temperature, inlet partial pressure of SiH_4, total pressure, and channel dimension [5,6].

Comparisons of the CKM model with experimental in situ laser-diagnostic measurements [53,54] were complicated somewhat by differences between the idealized flow in the model and the actual flow in the experiment. The experimental cell was a semi-circular channel with viewing windows on the side and top for laser-based diagnostic measurements. For the purposes of modeling, the cell was approximated as flow between two infinitely-wide flat plates. Predictions of the model of CKM compared well with the measurements of gas-phase temperature profiles [53], SiH_4 density profiles (at atmospheric and reduced total pressures) [53], and relative density profiles of the intermediate species Si_2 [53] and Si [54]. However, complete quantitative agreement was not obtained, and it was difficult to distinguish between errors introduced by the simplified geometry in the model and errors in the chemical mechanism. Clearly, it is most desirable to test detailed-chemistry CVD models with an experimental apparatus that closely approximates the simple, idealized flows required by the models.

In this paper, we present Si deposition rate measurements in a CVD cell that has been designed to have a well-characterized, simple geometry producing an ide-

alized, two-dimensional, axisymmetric flow. We present deposition-rate data along with a complete specification of reactor dimensions, flow rates, deposition-temperature profiles, pressure, and reactant concentrations. Such data allow rigorous tests of the chemical mechanisms of existing and future Si CVD models without the aforementioned fluid mechanics complications.

This paper also compares our experimental deposition rates with the rates calculated by the CKM model. We present two sets of model calculations, differing in the assumed probabilities for SiH_4 and Si_2H_6 reacting upon collision with the surface. The first calculation, termed Model 1, uses a previously published gas-phase reaction mechanism and surface reaction probabilities [24]. The second calculation, Model 2, differs only in that the surface reaction probabilities for SiH_4 and Si_2H_6 were extracted from the recent work of Buss, et al. [55]. Other parameters and rate constants in the Models were not adjusted to optimize agreement with the experimental deposition rates.

The next section describes the experimental two-dimensional deposition cell and gives all relevant experimental parameters. The CKM model and reaction mechanisms are discussed in the following section. The experimental deposition rates and model comparisons are then presented and discussed.

Experiment

A schematic of the apparatus, consisting of a vertical, axially-symmetric, heated flow tube with a special inlet design, is shown in Fig. 1. The symmetry of the tube flow ensures a truly two-dimensional geometry. All the necessary boundary conditions for accurate numerical simulation of the fluid mechanics can be supplied from knowledge of the exact form of the inlet velocity, the pressure, temperature profile measurements along the walls of the tube, and inlet gas partial pressures.

The lower chamber of the reactor is designed to produce a velocity front that is uniform across the tube radius at the beginning of the flow tube (2.5 cm outside diam). The bottom part of the cell is constructed of Pyrex and consists of a stagnation chamber made from 10 cm diam tubing terminated at one end with a window and joined at the other end to the flow tube as shown. A gas inlet tube penetrates the wall of the stagnation chamber and is bent into a circle with many small holes drilled in the walls to produce a gas diffuser. The flow tube extends roughly halfway into the 10 cm length of the stagnation chamber and is flared slightly at its end.

The flow tube extends roughly 1 m beyond the stagnation chamber to ensure a fully-developed parabolic velocity profile of the gas before it enters the heated region. Laser velocimetry measurements using the apparatus described in Ref. 56 were made to verify that the carrier gas did indeed develop into the expected Poiseuille flow which can be calculated from the measured total volume flow rate of the gas.

Deposition was made directly on the inside surface of a 2.5 cm outside diam., 2.17 cm inside diam., 60 cm long, fused quartz tube that was joined with a vacuum fitting to the Pyrex assembly described above. The quartz tube was heated with a tubular single-zone resistance furnace 36 cm long. Pressure was measured with a capacitance manometer at the gas-exit end of the tube. The apparatus was oriented vertically, and the gas flowed upward.

Surface temperature profiles along the inside of the flow tube were measured with type K (chromel-alumel) thermocouples. In one set of experiments, an exposed-junction, 1/16 in. diam. sheathed thermocouple probe with 0.010 in. diam. wire was used. Several runs were repeated to verify that the furnace produced the same profile for the identical temperature setting and flow conditions.

To verify that the thermocouple probe measurements did not contain significant errors due either to poor thermal contact with the surface or to conductive and radiative losses, another specialized tube was constructed. This tube contained embedded 0.003 in. diam. thermocouple junctions placed every 4 cm. The thermocouples were pushed through holes drilled in the side of the tube and were cemented into place with ceramic adhesive such that their junctions protruded one wire diameter above the inside surface of the tube. Temperature profiles obtained with this arrangement agreed with the probe measurements with an average deviation of 10°C. Profiles from four runs having heater settings of 600°, 650°, 750°, and 850°C are presented in Table 1 and in Fig. 2 as Runs 1 through 4, respectively. These wall-temperature profiles were used as boundary conditions in the numerical simulations. Because fluid mechanics models handle such boundary conditions easily, no attempt was made to force the temperature profiles to more "idealized" shapes such as a step function from room temperature to a uniform deposition temperature. Such functions are useful for analytic solutions, but are not necessary (and perhaps inappropriate due to the discontinuity) for numerical methods.

The quartz tubes were cleaned prior to deposition with chromic acid, rinsed in distilled water, and air dried. The deposition procedure consisted of mounting the quartz tube, allowing the system to come to steady-state at the desired heater temperature setting and carrier gas flow rate, and then introducing silane at a measured flow rate for a measured period of time. After cooling, parts of the tube where no deposition occured were cut off and the tube was then sectioned into quarters along its length. The inside surface of one of these sections was masked with thermoplastic using a template having 5 mm holes on 1 cm spacings. The unmasked silicon was removed with a 50:50 mixture of concentrated HF and HNO_3, producing an etch pattern with sharp steps every 5 mm along the length of the section. The deposited silicon film thickness was measured with a profilometer and deposition rates were calculated from the deposition

time. Rates for deposition times ranging from 10 to 40 minutes were used at one set of conditions to verify that the rate was linear in time.

A small systematic overestimation of the deposition rate data results because the etch process is not perfectly selective. Etch rates for quartz were found to be 100 Å/sec, whereas the silicon etch rate was roughly 1 micron/sec. The lowest measured deposition rates typically involved a measured step height of only 1000 Å which is not significantly larger than the ~500 Å of etching expected from a typical 5 sec dip in the etch bath. This would cause the deposition rate to be over-reported by 10^{-3} microns/min for the typical run times used. Since the etch dip times varied for each run and were not measured, no attempt has been made to correct for this systematic error.

For each of the four heater settings given in Table 1, two or three deposition runs were made. In each case, 10.34 SLM of Helium carrier (Spectra gases, 99.9999%) was mixed with 2.15 sccm electronic grade silane (Spectra gases, less than 1ppm impurities, including hydrogen) at a nominal pressure of 620 Torr. Each deposition run differed slightly in the total pressure, and, because mass flow controllers were used, the inlet average gas velocities also differed slightly from the nominal value of 62 cm/sec. (See next section for more details.)

Details of Calculation

Model 1– The model of Coltrin, Kee, and Miller has been described in detail elsewhere [5,6]. The model solves the boundary-layer equations for the fluid flow coupled to species conservation equations for chemical production and destruction and convective and diffusive transport. A primary assumption of the boundary layer equations is that diffusive transport is negligible compared to convective transport in the principal flow

direction. The model includes temperature-dependent transport properties, multicomponent ordinary diffusion, as well as thermal diffusion [6]. The model is restricted to two spatial dimensions, but the equations were presented in a form applicable for either axisymmetric flow or planar flow [5,6].

The model includes a detailed reaction mechanism describing the thermal decomposition of the reactant SiH_4 and subsequent reactions of intermediate species. The original model contained a 20-step gas-phase reaction mechanism, involving 15 chemical species [5]. This mechanism was further refined in Ref. 6. Recently, the reaction mechanism was extended [24] to reflect the most recent experimental and theoretical work on SiH_4 kinetics and thermochemistry, and contains 27 elementary reactions of 17 chemical species. The gas-phase reaction mechanism in Ref. 24 was used for the modeling in this paper. (See Ref. 24 for complete details of the reaction mechanism.)

In the models of Coltrin, et al. [5,6,24], surface reactions were treated in a rather simple way as boundary conditions on the gas-phase species concentrations. For each Si-containing species, they specified the probability that each species would react upon collision with the surface to deposit Si and evolve H_2 into the gas. The reactive-sticking coefficient (RSC) for each of the intermediate species SiH_3, SiH_2, SiH, Si, Si_2H_5, H_2SiSiH_2, H_3SiSiH, Si_2H_3, Si_2H_2, Si_2, and Si_3 was assumed to be very high, and, in the absense of experimental data, was set equal to one. Recently it has been verified that the RSC for one such reactive intermediate, SiH, is at least 0.94 [57].

In Refs. 6 and 24 the RSC for SiH_4 was set equal to

$$\gamma(SiH_4) = 5.37 \times 10^{-2} e^{-9400/T}. \qquad (1)$$

This expression was obtained by fitting the model deposition rate to an experimental deposition rate [58] at low temperature in a H_2 carrier gas. The activation energy of

18.7 kcal/mole chosen for the RSC was taken from the only available silane surface reactivity measurement [59]. In the original CKM models, the RSC for Si_2H_6 was assumed to be zero. However, recent experiments [55,60] showed that Si_2H_6 is actually about ten times more reactive at the surface than SiH_4. For this reason in Ref. 24 Coltrin, et al. used the expression

$$\gamma(Si_2H_6) = 5.37 \times 10^{-1} e^{-9400/T}. \quad (2)$$

for the Si_2H_6 RSC. For atmospheric pressure Si deposition, addition of the nonzero Si_2H_6 RSC made a negligible change to the deposition rate [24], and so none of the previous conclusions in Refs. 5 or 6 were affected. (Although Si_2H_6 is formed as an intermediate in the SiH_4 pyrolysis, it is also very reactive in the gas-phase. Most of the Si_2H_6 formed decomposes before it strikes the surface.)

Model 2– Buss, et al. [55] recently performed a molecular beam/surface scattering experiment to investigate the SiH_4 RSC. They found that the SiH_4 RSC did not follow simple Arrhenius behavior, but was a complicated function of both temperature and beam flux (pressure). Measurements yielded RSC's that were roughly proportional to $P^{-1/2}$ at low (710° C) temperatures, but were independent of P at high temperatures (1040° C). In addition, there were also indications that heated silane has a larger RSC than room temperature silane. The RSC for Si_2H_6 was also found to have a complicated temperature and flux dependence, and to be roughly ten times larger than SiH_4.

Since the complete pressure and temperature dependence of the silane RSC is not known at this time, we have chosen as a best estimate to use a typical RSC from data corresponding to conditions closest to those at atmospheric pressure. Buss, et al. compiled a number of sets of SiH_4 RSC's extracted from LPCVD deposition rate data at 625°C. (At this temperature, under LPCVD conditions, there should be little homogeneous SiH_4 decomposition, so the deposition rate is primarily due to the SiH_4

surface reaction.) From the LPCVD data compilation (Fig. 9 of Ref. 55) we estimate the SiH_4 RSC to be in the neighborhood of 5×10^{-5} at 625°C for the flux (3×10^{19} molecules cm^{-2} sec^{-1}) corresponding to the tube inlet partial pressure of silane (0.13 Torr). This value is roughly 33 times larger than the RSC of Eq. (1).

To examine the effect of the larger value for the SiH_4 RSC on the deposition rate, we have performed the calculations with Model 2, which differs only in the values used for the SiH_4 and Si_2H_6 RSC, assuming typical 40 kcal/mole [61-63] activation energies in both cases:

$$\gamma(SiH_4) = 2.72 \times 10^5 e^{-20131/T} \tag{3}$$

$$\gamma(Si_2H_6) = 2.72 \times 10^6 e^{-20131/T}. \tag{4}$$

In general, one would expect that at low temperature, where gas-phase decomposition of the silane is slow, the higher values for the SiH_4 and Si_2H_6 RSC's will lead to large increases in the predicted deposition rates via the inhomogeneous mechanism.

Each of the four experimental deposition runs were simulated using Models 1 and 2 using the wall temperature profiles in Table 1 as boundary conditions. Because the total pressure was different for each experimental run, different average velocities were used as follows: for Run 1 $\overline{v}$=62.9 cm/s and P=0.804 atm; for Run 2 $\overline{v}$=62.4 cm/s and P=0.810 atm; for Run 3 $\overline{v}$=61.8 cm/s and P=0.818 atm; and for Run 4 $\overline{v}$=60.4 cm/s and P=0.837 atm. Since steps were taken to ensure that the velocity was fully developed before entering the heated region, it is not necessary to model the 1 meter entrance length. Rather, at the beginning of the deposition region, one can assume a fully-developed (parabolic) velocity profile which has an average velocity corresponding to the experimental value. The deposition rates as a function of distance along the tube were calculated using Models 1 and 2 for each of the four runs. The models calculate the flux of silicon to the surface in units of mass per area per unit time and assume an

ideal density of 2.33 g/cm^3 for the deposited material to calculate a deposition rate. Therefore, a source of disagreement between model and experiment will be introduced if the morphology of the deposited film is such that the density differs from this value.

Experimental Deposition Rates

Experimental deposition rates for the four run conditions given in Table 1 are presented as the solid squares in figures 3-6. For each heater setting, at least two experimental runs are given to display the uncertainties in the deposition rates. Tables 2 through 10 list the data plotted in figures 3-6. Each of the deposition experiments had slightly different total pressures and average volume flow rates. These conditions were as follows: Run 1a, 611 Torr, 62.9 cm/s; Run 1b, 623 Torr, 61.7 cm/s; Run 2a, 616 Torr, 62.4 cm/s; Run 2b, 615 Torr, 62.4 cm/s; Run 3a, 623 Torr, 61.6 cm/s; Run 3b, 621 Torr, 61.8 cm/s; Run 3c, 620 Torr, 61.9 cm/s; Run 4a, 628 Torr, 61.1 cm/s; Run 4b, 636 Torr, 60.4 cm/s.

Each of the deposits in Runs 1 through 4 had a different appearance. Run 1 deposits were smooth and specular, ending in a soft, non-adherent film at roughly 45 cm. Run 2 had specular deposits that gradually turned hazy farther downstream. At 43 cm downstream, a black-brown film started abruptly. This film was too soft to be profiled. It is possible that these soft films are actually agglomerated particles generated upstream that have been forced to the surface by thermophoretic forces as the gas temperature gradient switches from a negative to a positive slope. Runs 3 and 4 both exhibited a specular region with an abrupt change to a hazy grey deposit that gradually returned to a specular film farther downstream. As mentioned earlier, there is a small systematic error in the experimental deposition rates due to overetching. The low temperature data in Run 1 (Fig. 3) is most affected by this overetch, because thinner overall films were deposited.

Fig. 2 shows that as one progresses from Run 1 to 4, the surface temperature increases more rapidly and reaches a higher maximum temperature. This leads to deposition earlier in the tube and an increase in the maximum deposition rate, as seen in the data of Figs. 3-6. The maximum in the deposition rate occurs at 37 cm downstream for Run 1 and decreases to 22 cm for Run 4. The overall shapes of the deposition data basically reflect the peaking of the temperature profiles in the tube for the low temperature Runs 1 and 2. However, for the high temperature Runs 3 and 4, the deposition rate peaks before the maximum in the temperature profile, and the deposition profile is less rounded. The sharper peak in the high temperature profiles is probably due to two effects. First is depletion of SiH_4; the higher integrated deposition along the tube depletes the amount of reactant available, causing the deposition rate to drop. Second is the homogeneous gas-phase nucleation of silicon particulates which is known to occur in helium carrier gas at high temperatures. Production of particles, which would be swept down-stream, would also contribute to depletion of silane and would result in a further decrease in the deposition rate.

Runs 1 (Fig. 3) and 3 (Fig. 5) both exhibit apparently increased deposition rates at the end of the tube. This probably indicates that a less dense film is being deposited rather than an increase in deposition rate. Note that this increase is not seen in Fig. 4 because the film was so soft past 43 cm that it could not be profiled. If the density of these soft films differs from the 2.33 g/cm^3 assumed in the model, one would not expect the model to match the measured deposition rates in these regions.

Comparisons with Model Predictions

Comparisons between predictions of Models 1 and 2 for the conditions of Runs 1 through 4 are also given in Figs. 3 through 6, respectively. In general, the model predictions follow experimental trends in the deposition rates. However, Model 2 predictions are brought into closer agreement with all experiments by using the SiH_4 and Si_2H_6 RSC's derived from the work of reference 55.

For the low temperature Runs 1 and 2, we expect the difference between Models 1 and 2 to be most noticeable because little gas-phase chemistry occurs at these temperatures. This is verified by the results in Figs. 3 and 4, in which Model 1 not only underpredicts the deposition rate, but also lags behind Model 2 and the experimental data by several centimeters. Model 2 does a very good job of predicting the overall shape, position, and magnitude of deposition for Runs 1 and 2. The shape of the deposition profile directly reflects the temperature profile; deposition turns on when the wall temperature is about 500° C, peaks at the temperature maximum at 37 cm, and decreases as the temperature drops.

For the high temperature Runs 3 and 4, contributions from gas-phase chemistry become more important, and we expect the two models to be in closer argeement with one another, because the gas-phase mechanism is the same for both models. This is true to some extent, as seen in Figs. 5 and 6. Model 1 predicts basically the same magnitude and shape of the deposition rate profile as Model 2, but the position of the curve for Model 1 still lags behind Model 2 and the experimental data. This lag is because Model 1 underpredicts the deposition rate at the low-temperature "turn-on" portion of the temperature profile. Model 2 accurately predicts the position of the onset of deposition and the peaking of the profile before the maximum in the temperature profile, but the position of the peak in the deposition differs from the experimental data

by 1 to 2 cm. More noticably, both Models 1 and 2 fail to give an accurate description of the tail in the experimental deposition profile for the high temperature runs. The most likely cause of this deviation is the aforementioned production of silicon particles which would contribute an additional silane loss mechanism, thus depressing the silicon deposition rate. Particle nucleation mechanisms are not included in Models 1 or 2.

Discussion

The above comparisons clearly indicate that the RSC in Model 1, which was extracted from deposition rate data in a hydrogen carrier gas, is not appropriate for silicon deposition from silane in a helium carrier. This implies that the RSC of silane not only depends on temperature and silane flux, but also depends on hydrogen concentration. Buss, et al. [55] observed less than a factor of two decrease in the silane RSC when a ten-fold excess of hydrogen was added to the silane. However, by comparing Eqs. (1) and (3) at 625° C it appears that the silane RSC in an atmosphere of hydrogen is over 30 times smaller than in a helium carrier.

The model calculations allow one to examine the relative roles of gas and surface chemistry in the silicon deposition. The contribution to silicon deposition from silane surface reactions at the deposition rate maximum is calculated to be 8% for Model 1 and 74% for Model 2 at Run 1 conditions, and 2.5% for Model 1 and 57% for Model 2 at Run 2 conditions. Since Model 2 provides a closer agreement with experimental results, one may conclude that surface chemistry reactions are dominant, but not totally responsible for silicon deposition at the low temperature Runs 1 and 2. For the high temperature Runs 3 and 4, very similar curves are obtained for Models 1 and 2, but dramatically different mechanisms are involved. Silane surface reactions contribute 0.4% for Model 1 and 46% for Model 2 at Run 3 conditions and 0.6% for Model 1 and 21% for Model 2 at Run 4 conditions. Model 1 results imply that the high temperature

runs are totally dominated by gas phase reactions, but Model 2 implies that there is still a significant contribution from surface reactions at these temperatures. These results serve to point out the pitfalls that one could encounter by empirically fitting a set of parameters to a specific deposition mechanism. Deposition rate data alone are not necessarily sufficient to distinguish subtle effects that occur in the complex deposition process. We have therefore refrained from any ad hoc adjustments to the parameters in the models to obtain better agreement with deposition rates.

Buss, et al. [55] found that the RSC for disilane was roughly ten times that of silane. Since disilane is formed in the gas-phase decomposition of silane, it is important to examine the contribution to deposition from disilane surface reactions. At the deposition rate maximum, disilane surface reactions contribute at Run 1 through 4 conditions 1.5%, 0.5%, 0.03%, and 0.04% for Model 1, and 8%, 7%, 2.7%, and 0.2% for Model 2, respectively. Our results therefore imply that disilane never dominates in atmospheric pressure silicon deposition from silane, but it is not negligible at low temperatures. These results can be explained from the fact that disilane is even more unstable than silane in the gas phase. Conditions that favor the decomposition of silane, which are required in order to form disilane, also favor the rapid decomposition of disilane as it is transported toward the surface through a steep temperature gradient. The competition between the large disilane RSC and the small amount of disilane that reaches the surface thus is not predicted to dominate silane surface reactions with the current models.

If no silane depletion were to occur as silicon is deposited along the tube, it would be valid to use the temperature profile data in Table 1 to identify a temperature for each distance and construct an Arrhenius plot of deposition rate vs. 1/T for the run conditions 1 through 4. Although this is not stictly the case, the results of such a plot,

Fig. 7, are informative. (Only data up to the deposition maximum have been included to minimize effects of depletion.) Also plotted are equivalent curves from Models 1 and 2. Except at the low temperatures where overetching errors dominate, all experimental runs fall on a line corresponding to a 37 kcal/mole activation energy. A similar plot for Model 1 does not result in the data falling on a single line. The slopes of the curves for Model 1 are steeper than the experimental data. This is because the gas-phase reaction rates, which have higher activation energies, are dominating. Agreement with Model 2 is much better; the predicted curves fall practically on top of the experimental data and have a 37 kcal/mole activation energy.

Conclusions

Comparisons of Models 1 and 2 with deposition rate measurements in a two-dimensional flow clearly indicate that the previously published reactive sticking coefficient formula for silane [5] (Model 1) is inappropriate to use for deposition that does not use a hydrogen carrier gas. Although the flux-dependence of the RSC [55] is not included, formulas in Eqns. 3 and 4, when coupled with the detailed model of Coltrin, Kee, and Miller, yield deposition rate predictions that are quite close to experimental measurements over a wide temperature range at nearly atmospheric pressure conditions. The correct surface chemistry is needed in the model even for high temperature conditions in which gas-phase chemistry is expected to dominate the deposition. This is because low temperature deposition that occurs upstream determines the concentration of chemical species and resulting depletion downstream. The experimental deposition rate data presented here provides the first measurements in a truly two dimensional flow with measured boundary conditions that can be used to rigorously test existing and future numerical CVD models.

Acknowledgments

We would like to thank Michael P. Youngman for playing a large role in the design of the apparatus and collection of the deposition rate data, as well as technical assistance in all aspects of the experimental work. We also thank Pauline Ho for many helpful discussions. This work was performed at Sandia National Laboratories for the Office of Basic Energy Science, supported by the U.S. Department of Energy under contract No.DE-AC04-76DP00789.

References

1. D. W. Hess, K. F. Jensen, and T. J. Anderson, *Rev. Chem. Eng.* **3**, 97 (1985).
2. K. F. Jensen, *Chem. Eng. Sci.* **42**, 923 (1987).
3. F. A. Kuznetsov and V. I. Belyi, *J. Electrochem. Soc.* **117**, 785 (1970).
4. G. H. Westphal, D. W. Shaw, and R. A. Hartzell, *J. Cryst. Growth* **56**, 324 (1982).
5. M. E. Coltrin, R. J. Kee, and J. A. Miller, *J. Electrochem. Soc.* **131**, 425 (1984).
6. M. E. Coltrin, R. J. Kee, and J. A. Miller, *J. Electrochem. Soc.* **133**, 1206 (1986).
7. G. Evans and R. Greif, *Int. J. Heat Mass Trans.* **32** 895 (1989).
8. F. C. Eversteijn and H. L. Peek, *Philips Res. Rep.* **25**, 472 (1970).
9. F. C. Eversteijn, P. J. W. Severin, C. H. J. van den Brekel, and H. L. Peek, *J. Electrochem. Soc.* **117**, 925 (1970).
10. J. van de Ven, G. M. J. Rutten, M. J. Raaijmakers, and L. J. Giling, *J. Cryst. Growth* **76**, 352 (1986).
11. P. C. Rundle, *J. Cryst. Growth* **11**, 6 (1971).
12. R. Takahashi, Y. Koza, and K. Sugawara, *J. Electrochem. Soc.* **119**, 1406 (1972).
13. S. V. Berkman, V. S. Ban, and V. Goldsmith, in "Heteroepitaxial Semiconductors for Electronic Devices," G. W. Cullen and C. C. Wang, Editors, Ch. 7, Springer-Verlag, New York (1977).
14. V. S. Ban, *J. Electrochem. Soc.* **125**, 317 (1978).
15. S. Rhee, J. Szekely, and O. J. Ilegbusi, *J. Electrochem. Soc.* **134**, 2552 (1987).
16. H. K. Moffat and K. F. Jensen, *J. Cryst. Growth* **77**, 108 (1986).
17. H. K. Moffat and K. F. Jensen, *J. Electrochem. Soc.* **135**, 459 (1988).
18. K. F. Jensen and D. B. Graves, *J. Electrochem. Soc.* **130**, 1950 (1983).
19. K. F. Roenigk and K. F. Jensen, *J. Electrochem. Soc.* **132**, 448 (1985).
20. M. L. Hitchman, J. Kane and A. E. Widmer, *Thin Solid Films* **59**, 231 (1979).

21. A. E. T. Kuiper, C. H. J. van den Brekel, J. de Groot, and F. W. Veltkamp, *J. Electrochem. Soc.* **129**, 2288 (1982).

22. S. Middleman and A. Yeckel, *J. Electrochem. Soc.* **133**, 1951 (1986).

23. K. F. Roenigk and K. F. Jensen, *J. Electrochem. Soc.* **134**, 1777 (1987).

24. M. E. Coltrin, R. J. Kee, and G. H. Evans, *J. Electrochem. Soc.* **136**, 819 (1989).

25. G. Evans and R. Greif, *Num. Heat Trans.* **14**, 373 (1988).

26. G. Evans and R. Greif, *J. Heat Trans.* **109**, 928 (1987).

27. G. Evans and R. Greif, *Num. Heat Trans.* **12**, 243 (1987).

28. M. L. Hitchman and B. J. Curtis, *J. Cryst. Growth* **60**, 43 (1982).

29. K. Chen and A. R. Mortazavi, *J. Cryst. Growth* **77**, 199 (1986).

30. M. E. Coltrin, R. J. Kee, G. Evans, and J. A. Miller, in "Chemical Vapor Deposition," G. W. Cullen, Editor, p. 33, The Electrochemical Society Softbound Proceedings Series, Princeton, NJ (1987).

31. K. Sugawara, *J. Electrochem. Soc.* **119**, 1749 (1972).

32. R. Pollard and J. Newman, *J. Electrochem. Soc.* **127**, 744 (1980).

33. M. Michaelidis and R. Pollard, *J. Electrochem. Soc.* **131**, 861 (1984).

34. J. P. Jenkinson and R. Pollard, *J. Electrochem. Soc.* **131**, 2911 (1984).

35. M. Tirtowidjojo and R. Pollard, J. Crystal Growth 93 (1988) 108.

36. Y. Kusumoto, T. Hayashi, and S. Komiya, *Jap. J. Appl. Phys.* **24**, 620 (1985).

37. C. Houtman, D. B. Graves, and K. F. Jensen, *J. Electrochem. Soc.* **133**, 961 (1986).

38. G. Wahl, F. Schmaderer, R. Huber, and R. Weber, in "Chemical Vapor Deposition," G. W. Cullen, Editor, p. 42, The Electrochemical Society Softbound Proceedings Series, Princeton, NJ (1987).

39. G. Wahl, in "Chemical Vapor Deposition," McD. Robinson, C. H. J. van den Brekel, G. W. Cullen, J. M. Blocher, Jr., and P. Rai-Choudhury, Editors, p. 60, The Electrochemical Society Softbound Proceedings Series, Princeton, NJ (1984).
40. G. Wahl, *Thin Solid Films* **40**, 13 (1977).
41. J. Juza and J. Cermak, *Chem. Eng. Sci.* **35**, 429 (1980).
42. J. Juza and J. Cermak, *J. Electrochem. Soc.* **129**, 1627 (1982).
43. E. Fujii, H. Nakamura, K. Haruna, and Y. Koga, *J. Electrochem. Soc.* **119**, 1106 (1972).
44. C. W. Manke and L. F. Donaghey, in "Chemical Vapor Deposition, L. F. Donaghey, P. Rai-Choudhury, and R. N. Tauber, Editors, p. 151, The Electrochemical Society Softbound Proceedings Series, Princeton, NJ (1977).
45. C. W. Manke and L. F. Donaghey, *J. Electrochem. Soc.* **124**, 561 (1977).
46. Y. He and Y. Sahai, in "Chemical Vapor Deposition," G. W. Cullen, Editor, p. 193, The Electrochemical Society Softbound Proceedings Series, Princeton, NJ (1987).
47. F. W. Dittman, *Adv. Chem. Ser.* **133**, 463 (1979).
48. W. H. Shepherd, *J. Electrochem. Soc.* **112**, 988 (1965).
49. S. E. Bradshaw, *Int. J. Electronics* **21**, 205 (1966).
50. M. E. Coltrin and R. J. Kee, *J. Crystal Growth*, to be submitted.
51. M. Tirtowidjojo and R. Pollard, *J. Crystal Growth* **93**, 108 (1988).
52. T. J. Mountziaris and K. F. Jensen, *Mater. Res. Soc. Symp. Proc.* **131**, 117 (1988).
53. W. G. Breiland, M. E. Coltrin, and P. Ho, *J. Appl. Phys.* **59**, 3267 (1986).
54. W. G. Breiland, P. Ho, and M. E. Coltrin, *J. Appl. Phys.* **60**, 1505 (1986).
55. R. J. Buss, P. Ho, W. G. Breiland, and M. E. Coltrin, *J. Appl. Phys.*, **63**, 2808 (1988).

56. W. G. Breiland and P. Ho, in "Chemical Vapor Deposition," McD. Robinson, C. H. J. van den Brekel, G. W. Cullen, J. M. Blocher, Jr., and P. Rai-Choudhury, Editors, p. 44, The Electrochemical Society Softbound Proceedings Series, Princeton, NJ (1984).

57. P. Ho, W. G. Breiland, and R. J. Buss, *J. Chem. Phys.*, **91**, 2627 (1989).

58. C. H. J. van den Brekel, Ph. D. Thesis, University of Nijmegen, Nijmegen, The Netherlands (1978).

59. B. A. Joyce, R. R. Bradley, and G. R. Booker, *Philos. Mag.*, **15**, 1167 (1967).

60. S. M. Gates, *Surf. Sci.*, **195**, 307 (1988).

61. W. A. P. Claassen, J. Bloem, W. G. J. N. Valkenburg, and C. H. J. van den Brekel, *J. Crystal Growth* **57**, 259 (1982).

62. D. W. Foster, A. J. Learn, and T. I. Kamins, *J. Vac. Sci. Technol.* **B4**, 1182 (1986).

63. R. S. Rosler, *Solid State Technol.* **April**, 63 (1977).

Table 1: Reactor Wall Temperature Along Flow Direction

Distance (cm)	Run 1 T (°C)	Run 2 T (°C)	Run 3 T (°C)	Run 4 T (°C)
0	22	20	25	29
1	23	21	26	30
2	24	22	27	31
3	24	23	28	31
4	25	24	28	31
5	26	25	29	33
6	27	26	30	34
7	29	28	32	38
8	33	31	37	43
9	47	41	48	57
10	80	71	79	105
11	108	108	137	166
12	137	138	185	230
13	169	180	233	288
14	206	229	293	364
15	246	276	350	424
16	281	316	396	477
17	319	355	441	526
18	348	387	479	573
19	372	415	513	611
20	399	447	545	648
21	422	473	571	680
22	443	493	597	705
23	463	514	619	730
24	480	535	642	754
25	497	553	659	775
26	512	568	675	793
27	527	583	691	810
28	540	596	705	826
29	553	608	716	839
30	564	620	727	851
31	574	630	737	862
32	583	639	746	872
33	592	648	752	879
34	598	655	758	886
35	604	660	762	891
36	608	663	764	893

37	609	664	763	892
38	608	662	760	889
39	605	658	754	883
40	599	652	744	873
41	589	640	730	858
42	575	625	713	837
43	555	604	689	812
44	532	579	659	781
45	509	550	628	754
46	484	516	593	731
47	465	459	522	710
48	390	423	481	671
49	331	378	422	606
50	274	295	350	489

Table 2: Deposition Rate Along Flow Direction (Run 1a)

Distance (cm)	Deposition Rate (μm/min)	Distance (cm)	Deposition Rate (μm/min)
24.35	1.98E-3	36.73	1.13E-2
24.84	1.82E-3	37.21	1.12E-2
25.29	1.85E-3	37.69	1.14E-2
25.77	2.19E-3	38.16	1.13E-2
26.25	1.98E-3	38.65	1.11E-2
26.73	2.14E-3	39.11	1.11E-2
27.19	2.37E-3	39.58	1.06E-2
27.69	2.37E-3	40.07	9.98E-3
28.17	2.85E-3	40.55	9.38E-3
28.64	2.71E-3	41.02	8.55E-3
29.11	3.46E-3	41.49	8.10E-3
29.58	3.36E-3	41.97	7.45E-3
30.05	3.52E-3	42.45	6.76E-3
30.54	4.14E-3	42.93	5.87E-3
31.00	5.22E-3	43.40	5.50E-3
31.49	5.16E-3	43.88	4.97E-3
31.96	6.78E-3	44.36	5.10E-3
32.45	6.36E-3	44.84	4.81E-3
32.91	6.82E-3	45.30	4.90E-3
33.39	7.63E-3	45.80	5.24E-3
33.86	8.06E-3	46.26	4.93E-3
34.35	9.36E-3	46.75	4.99E-3
34.82	8.97E-3	47.21	4.21E-3
35.30	1.02E-2	47.70	4.31E-3
35.79	1.03E-2	48.18	3.52E-3
36.26	1.10E-2	48.66	3.23E-3

Table 3: Deposition Rate Along Flow Direction (Run 1b)

Distance (cm)	Deposition Rate (μm/min)	Distance (cm)	Deposition Rate (μm/min)
24.35	1.43E-3	35.79	1.09E-2
24.84	1.59E-3	36.26	1.15E-2
25.29	1.51E-3	36.73	1.17E-2
25.77	1.71E-3	37.21	1.18E-2
26.25	2.09E-3	37.69	1.18E-2
26.73	1.95E-3	38.16	1.17E-2
27.19	1.88E-3	38.65	1.16E-2
27.69	2.47E-3	39.11	1.11E-2
28.17	2.67E-3	39.58	1.07E-2
28.64	2.99E-3	40.07	9.8E-3
29.11	3.18E-3	40.55	9.75E-3
29.58	3.48E-3	41.02	8.32E-3
30.05	4.18E-3	41.49	8.05E-3
30.54	4.17E-3	41.97	6.93E-3
31.00	5.05E-3	42.45	6.61E-3
31.49	5.25E-3	42.93	5.54E-3
31.96	5.74E-3	43.40	5.14E-3
32.45	6.41E-3	43.88	4.93E-3
32.91	7.10E-3	44.36	4.67E-3
33.39	8.14E-3	44.84	4.99E-3
33.86	8.50E-3	45.30	4.87E-3
34.35	8.82E-3	45.80	5.50E-3
34.82	9.76E-3	46.26	4.52E-3
35.30	9.99E-3	46.75	6.68E-3

Table 4: Deposition Rate Along Flow Direction (Run 2a)

Distance (cm)	Deposition Rate (μm/min)	Distance (cm)	Deposition Rate (μm/min)
22.35	2.85E-3	32.82	3.81E-2
22.84	2.97E-3	33.30	4.08E-2
23.29	3.17E-3	33.79	4.06E-2
23.77	3.64E-3	34.26	4.33E-2
24.25	3.77E-3	34.73	4.57E-2
24.73	4.32E-3	35.21	4.84E-2
25.19	3.78E-3	35.69	4.76E-2
25.69	5.03E-3	36.16	4.99E-2
26.17	5.44E-3	36.65	4.63E-2
26.64	5.42E-3	37.11	5.04E-2
27.11	6.54E-3	37.58	5.04E-2
27.58	7.61E-3	38.07	4.74E-2
28.05	8.22E-3	38.55	4.36E-2
29.00	9.57E-3	39.02	4.05E-2
29.49	1.32E-2	39.49	3.80E-2
29.96	1.69E-2	39.97	3.54E-2
30.45	1.86E-2	40.45	3.12E-2
30.91	2.08E-2	40.93	2.81E-2
31.39	2.40E-2	41.40	2.46E-2
31.86	2.73E-2	41.88	2.41E-2
32.35	2.98E-2	42.36	2.75E-2

Table 5: Deposition Rate Along Flow Direction (Run 2b)

Distance (cm)	Deposition Rate (μm/min)	Distance (cm)	Deposition Rate (μm/min)
22.35	2.27E-3	32.82	3.62E-2
22.84	2.62E-3	33.30	4.15E-2
23.29	3.03E-3	33.79	4.42E-2
23.77	3.08E-3	34.26	4.87E-2
24.25	3.66E-3	34.73	5.20E-2
24.73	3.66E-3	35.21	5.14E-2
25.19	4.11E-3	35.69	5.31E-2
25.69	5.03E-3	36.16	5.46E-2
26.17	5.62E-3	36.65	5.20E-2
26.64	6.17E-3	37.11	5.50E-2
27.11	7.20E-3	37.58	5.36E-2
27.58	7.56E-3	38.07	5.17E-2
28.05	8.74E-3	38.55	5.02E-2
28.54	9.46E-3	39.02	4.56E-2
29.00	1.21E-2	39.49	4.22E-2
29.49	1.39E-2	39.97	3.96E-2
29.96	1.65E-2	40.45	3.57E-2
30.45	1.96E-2	40.93	3.21E-2
30.91	2.23E-2	41.40	2.92E-2
31.39	2.54E-2	41.88	2.65E-2
31.86	2.87E-2	42.36	2.58E-2
32.35	3.34E-2		

Table 6: Deposition Rate Along Flow Direction (Run 3a)

Distance (cm)	Deposition Rate (μm/min)	Distance (cm)	Deposition Rate (μm/min)
18.35	4.02E-3	31.69	6.79E-2
18.84	3.31E-3	32.16	6.29E-2
19.29	3.28E-3	32.65	6.00E-2
19.77	3.47E-3	33.11	5.66E-2
20.25	4.01E-3	33.58	5.40E-2
20.73	4.82E-3	34.07	5.14E-2
21.19	6.20E-3	34.55	4.69E-2
21.69	6.81E-3	35.02	4.44E-2
22.17	7.96E-3	35.49	4.15E-2
22.64	1.05E-2	35.97	3.90E-2
23.11	1.20E-2	36.45	3.52E-2
23.58	1.72E-2	36.93	3.40E-2
24.05	2.02E-2	37.40	3.15E-2
24.54	2.86E-2	37.88	2.87E-2
25.00	3.52E-2	38.36	2.64E-2
25.49	4.44E-2	38.84	2.42E-2
25.96	4.88E-2	39.30	2.34E-2
26.45	5.47E-2	39.80	2.10E-2
26.91	6.34E-2	40.26	2.00E-2
27.39	7.70E-2	40.75	1.77E-2
27.86	8.59E-2	41.21	1.75E-2
28.35	9.21E-2	41.70	1.56E-2
28.82	9.41E-2	42.18	1.48E-2
29.30	9.38E-2	42.66	1.37E-2
29.79	9.08E-2	43.12	1.40E-2
30.26	8.38E-2	43.60	1.57E-2
30.73	8.00E-2	44.08	2.03E-2
31.21	7.47E-2		

Table 7: Deposition Rate Along Flow Direction (Run 3b)

Distance (cm)	Deposition Rate (μm/min)	Distance (cm)	Deposition Rate (μm/min)
18.35	3.26E-3	31.69	6.51E-2
18.84	3.01E-3	32.16	6.24E-2
19.29	3.22E-3	32.65	5.81E-2
19.77	3.24E-3	33.11	5.58E-2
20.25	3.81E-3	33.58	5.21E-2
20.73	4.08E-3	34.07	4.88E-2
21.19	4.64E-3	34.55	4.52E-2
21.69	6.19E-3	35.02	4.26E-2
22.17	8.55E-3	35.49	3.96E-2
22.64	1.02E-2	35.97	3.63E-2
23.11	1.24E-2	36.45	3.32E-2
23.58	1.68E-2	36.93	3.09E-2
24.54	2.82E-2	37.40	2.83E-2
25.00	3.64E-2	37.88	2.64E-2
25.49	5.00E-2	39.30	2.11E-2
25.96	6.36E-2	39.80	1.88E-2
26.45	7.35E-2	40.26	1.85E-2
26.91	6.76E-2	40.75	1.66E-2
27.39	7.92E-2	41.21	1.57E-2
27.86	8.96E-2	41.70	1.39E-2
28.35	9.33E-2	42.18	1.32E-2
28.82	9.31E-2	42.66	1.19E-2
29.30	9.07E-2	43.12	1.09E-2
29.79	8.67E-2	43.60	1.03E-2
30.26	8.27E-2	44.08	1.25E-2
30.73	7.81E-2	44.57	1.52E-2
31.21	7.20E-2		

Table 8: Deposition Rate Along Flow Direction (Run 3c)

Distance (cm)	Deposition Rate (μm/min)	Distance (cm)	Deposition Rate (μm/min)
19.29	2.94E-3	32.16	6.25E-2
19.77	3.91E-3	32.65	5.84E-2
20.25	4.30E-3	33.11	5.66E-2
20.73	5.24E-3	33.58	5.16E-2
21.19	5.70E-3	34.07	4.88E-2
21.69	6.78E-3	34.55	4.52E-2
22.17	8.23E-3	35.02	4.33E-2
22.64	1.08E-2	35.49	3.96E-2
23.11	1.35E-2	35.97	3.76E-2
23.58	1.99E-2	36.45	3.40E-2
24.05	2.57E-2	36.93	3.24E-2
24.54	3.46E-2	37.40	2.93E-2
25.00	4.25E-2	37.88	2.80E-2
25.49	6.01E-2	38.36	2.48E-2
25.96	6.77E-2	38.84	2.40E-2
26.45	8.13E-2	39.30	2.13E-2
26.91	7.91E-2	39.80	2.04E-2
27.39	8.06E-2	40.26	1.79E-2
27.86	8.95E-2	40.75	1.71E-2
28.35	9.26E-2	41.21	1.60E-2
28.82	9.10E-2	41.70	1.51E-2
29.30	8.90E-2	42.18	1.36E-2
29.79	8.43E-2	42.66	1.25E-2
30.26	8.22E-2	43.12	1.16E-2
30.73	7.78E-2	43.60	1.29E-2
31.21	7.29E-2	44.08	1.59E-2
31.69	6.61E-2	44.57	2.27E-2

Table 9: Deposition Rate Along Flow Direction (Run 4a)

Distance (cm)	Deposition Rate (μm/min)	Distance (cm)	Deposition Rate (μm/min)
17.35	4.01E-3	27.35	5.57E-2
17.84	4.88E-3	27.82	5.16E-2
18.29	7.61E-3	28.30	4.52E-2
18.77	1.07E-2	28.79	3.64E-2
19.25	1.80E-2	29.26	3.16E-2
19.73	3.02E-2	29.73	2.88E-2
20.19	4.40E-2	30.21	2.53E-2
20.69	5.60E-2	30.69	2.16E-2
21.17	7.71E-2	31.16	1.89E-2
21.64	1.03E-1	31.65	1.65E-2
22.11	1.12E-1	32.11	1.37E-2
22.58	1.09E-1	32.58	1.18E-2
23.05	9.98E-2	33.55	1.06E-2
23.54	9.00E-2	34.02	8.72E-3
24.00	8.87E-2	34.49	7.87E-3
24.49	8.43E-2	34.97	6.37E-3
24.96	8.24E-2	35.45	5.67E-3
25.45	7.61E-2	35.93	5.23E-3
25.91	7.20E-2	36.40	4.70E-3
26.39	6.56E-2	36.88	3.94E-3
26.86	6.05E-2	37.36	3.58E-3

Table 10: Deposition Rate Along Flow Direction (Run 4b)

Distance (cm)	Deposition Rate (μm/min)	Distance (cm)	Deposition Rate (μm/min)
17.35	4.53E-3	27.82	5.32E-2
17.84	5.07E-3	28.30	4.76E-2
18.29	8.09E-3	28.79	4.52E-2
18.77	1.02E-2	29.26	4.20E-2
19.25	1.46E-2	29.73	4.39E-2
19.73	2.17E-2	30.21	3.59E-2
20.19	3.51E-2	30.69	3.11E-2
20.69	4.63E-2	31.16	2.70E-2
21.17	6.21E-2	31.65	2.27E-2
21.64	9.09E-2	32.11	2.00E-2
22.11	1.13E-1	32.58	1.65E-2
22.58	1.17E-1	33.07	1.43E-2
23.05	1.06E-1	33.55	1.19E-2
23.54	9.49E-2	34.02	1.09E-2
24.00	9.02E-2	34.49	9.08E-3
24.49	8.68E-2	34.97	8.08E-3
24.96	8.33E-2	35.45	6.95E-3
25.45	7.79E-2	35.93	6.06E-3
25.91	7.38E-2	36.40	5.36E-3
26.39	6.81E-2	36.88	4.97E-3
27.35	5.78E-2	37.36	4.04E-3

FIGURE CAPTIONS

FIG. 1. Schematic diagram of experimental reactor.

FIG. 2. Temperature profiles of the inside surface of the flow tube for Runs 1 through 4.

FIG. 3. Deposition rates and model predictions under the conditions of Run 1, Table 1.

FIG. 4. Deposition rates and model predictions under the conditions of Run 2, Table 1.

FIG. 5. Deposition rates and model predictions under the conditions of Run 3, Table 1.

FIG. 6. Deposition rates and model predictions under the conditions of Run 4, Table 1.

FIG. 7. Arrhenius plots of deposition rate vs 1000/T obtained by correlating the deposition rate at a given distance with the temperature from Table 1. Only data up to the deposition rate maximum is plotted. Experimental data: X, Run 1; diamond, Run 2; square, Run 3; circle, Run 4. Model results: solid, Run 1; dotted, Run 2; dashed, Run 3; dot-dashed, Run 4.

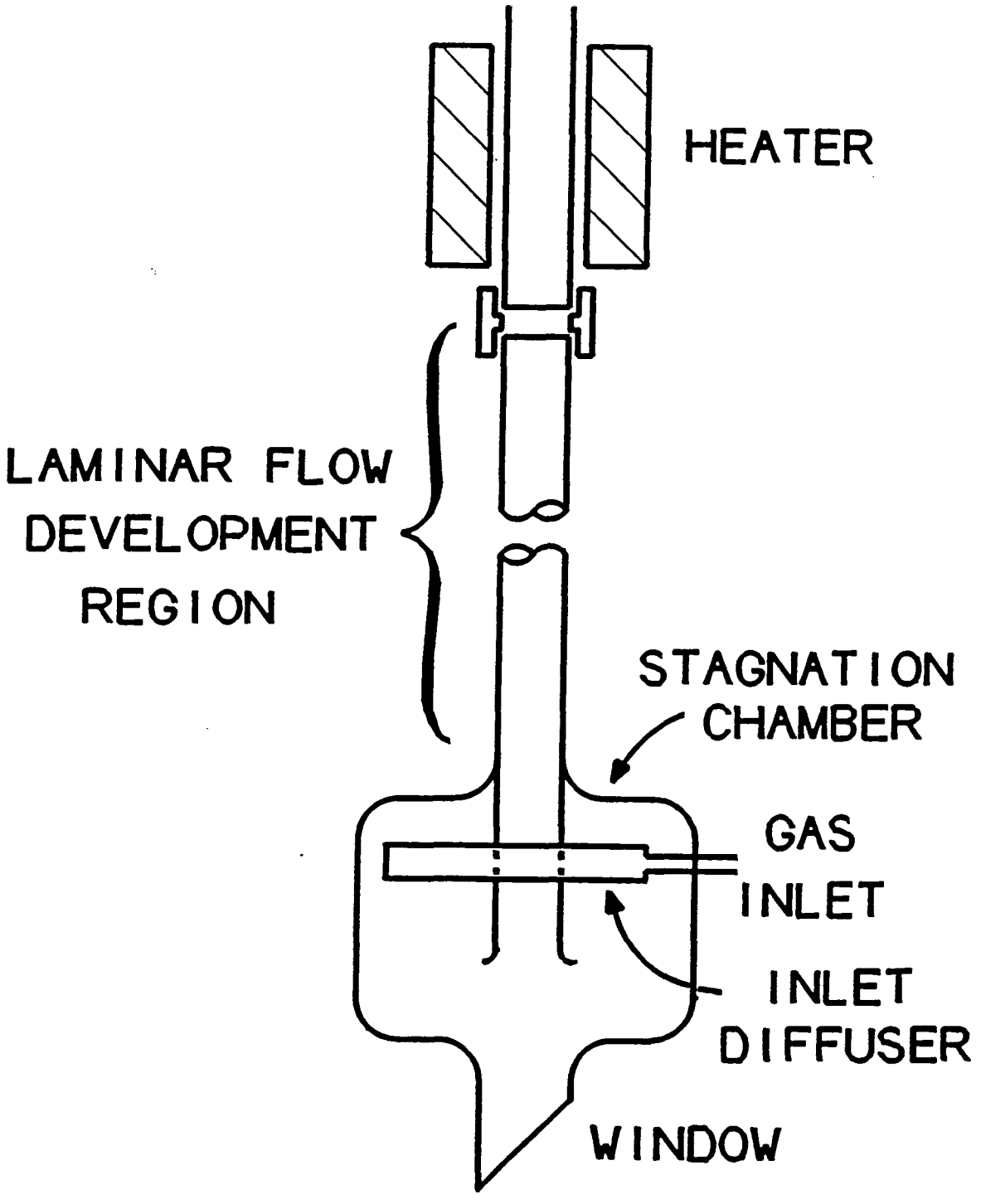
HEATER
LAMINAR FLOW
DEVELOPMENT
REGION
STAGNATION
CHAMBER
GAS
INLET
INLET
DIFFUSER
WINDOW

Fig. 1

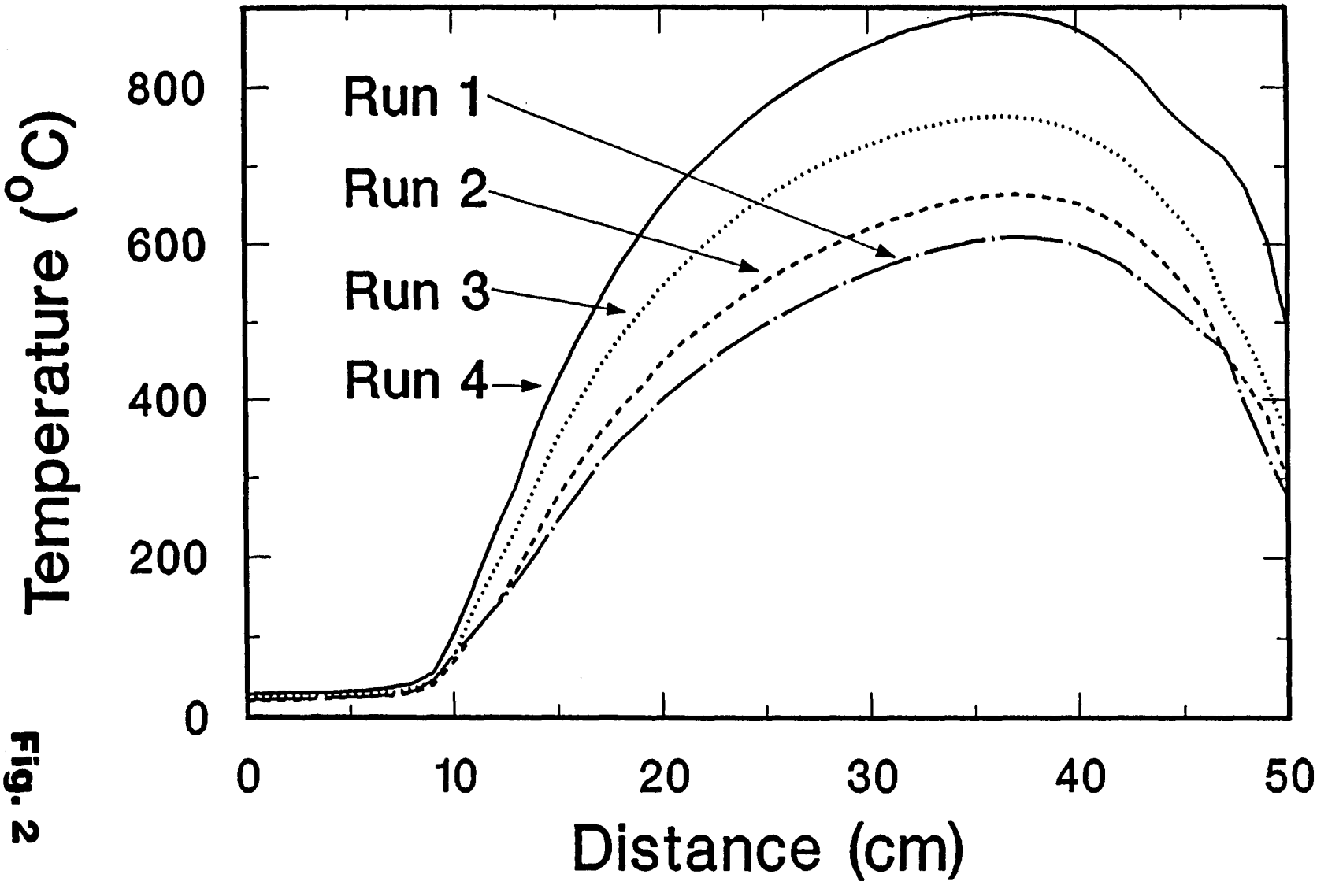
Temperature (°C)
800
600
400
200
0
Run 1
Run 2
Run 3
Run 4
0
10
20
30
40
50
Distance (cm)

Fig. 2

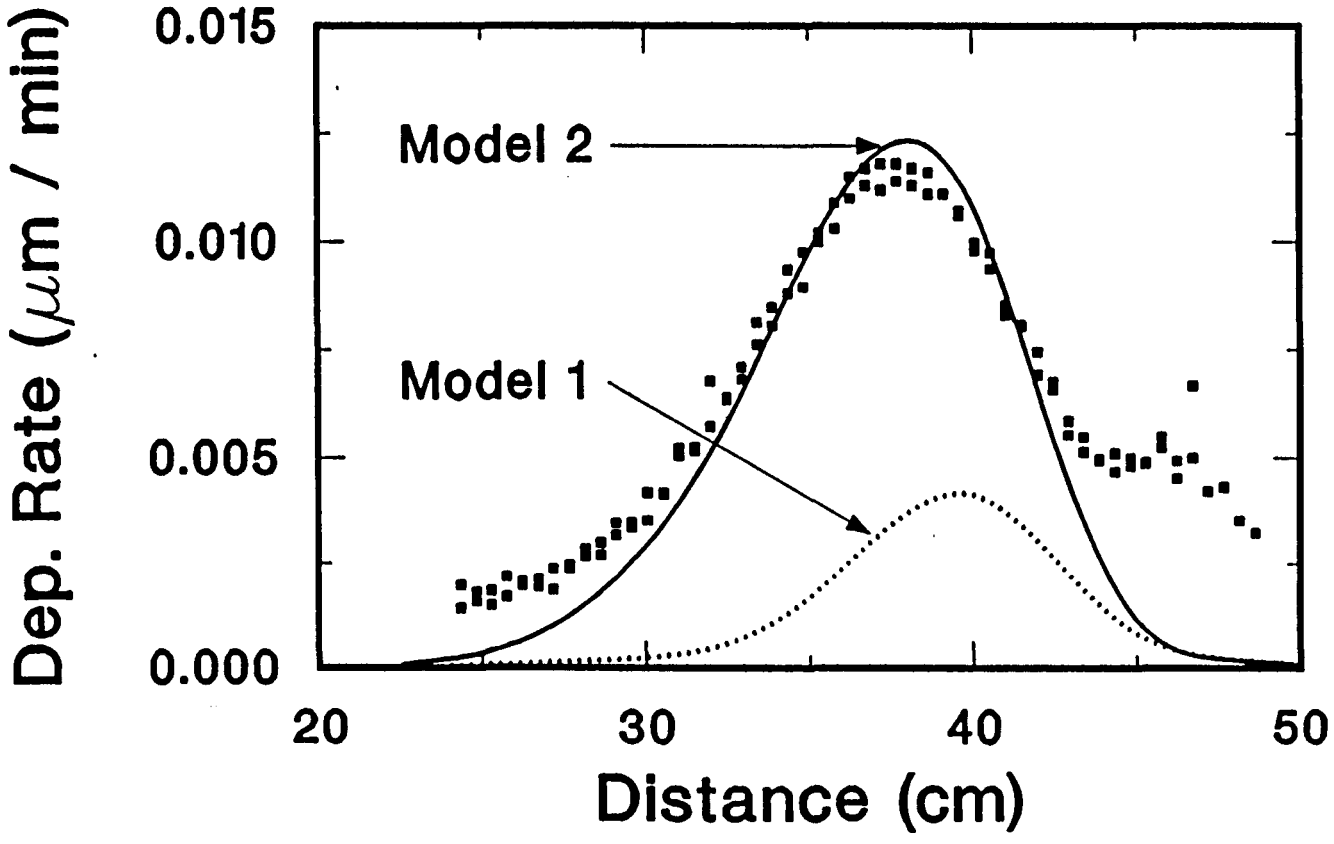
Dep. Rate (μm / min)
0.015
0.010
0.005
0.000
Model 2
Model 1
20
30
40
50
Distance (cm)

Fig. 3

Dep. Rate (μm / min)
0.06
0.04
0.02
0.00
Model 2
Model 1
20
30
40
50
Distance (cm)

Fig. 4

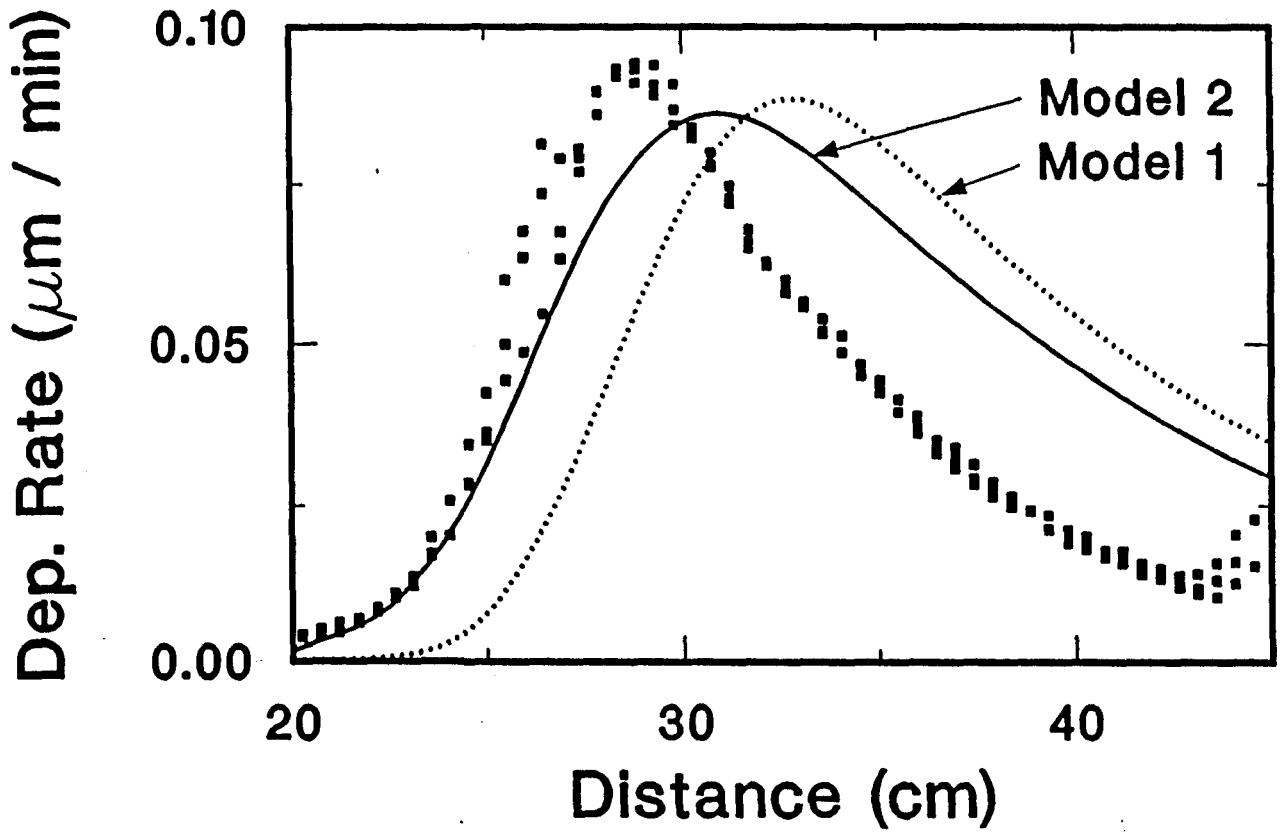

Fig. 5

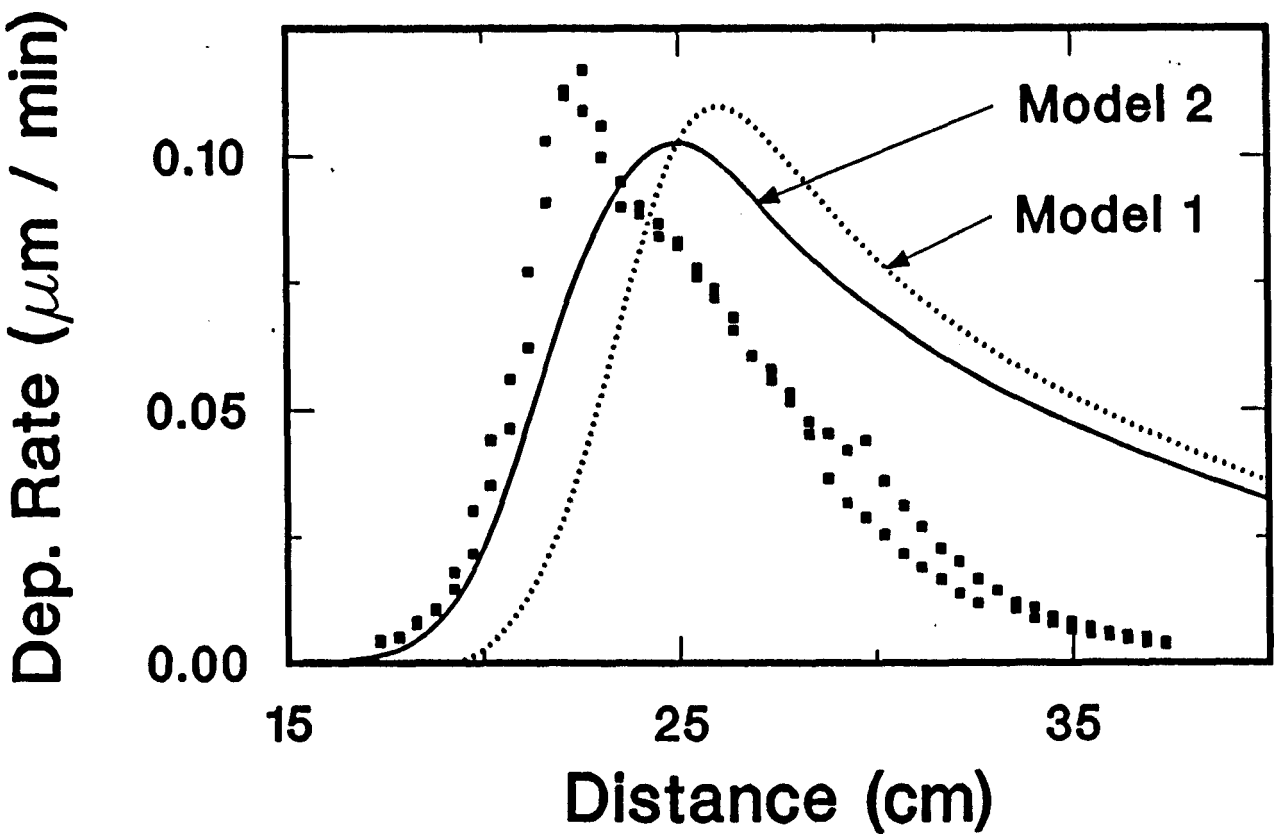

Fig. 6

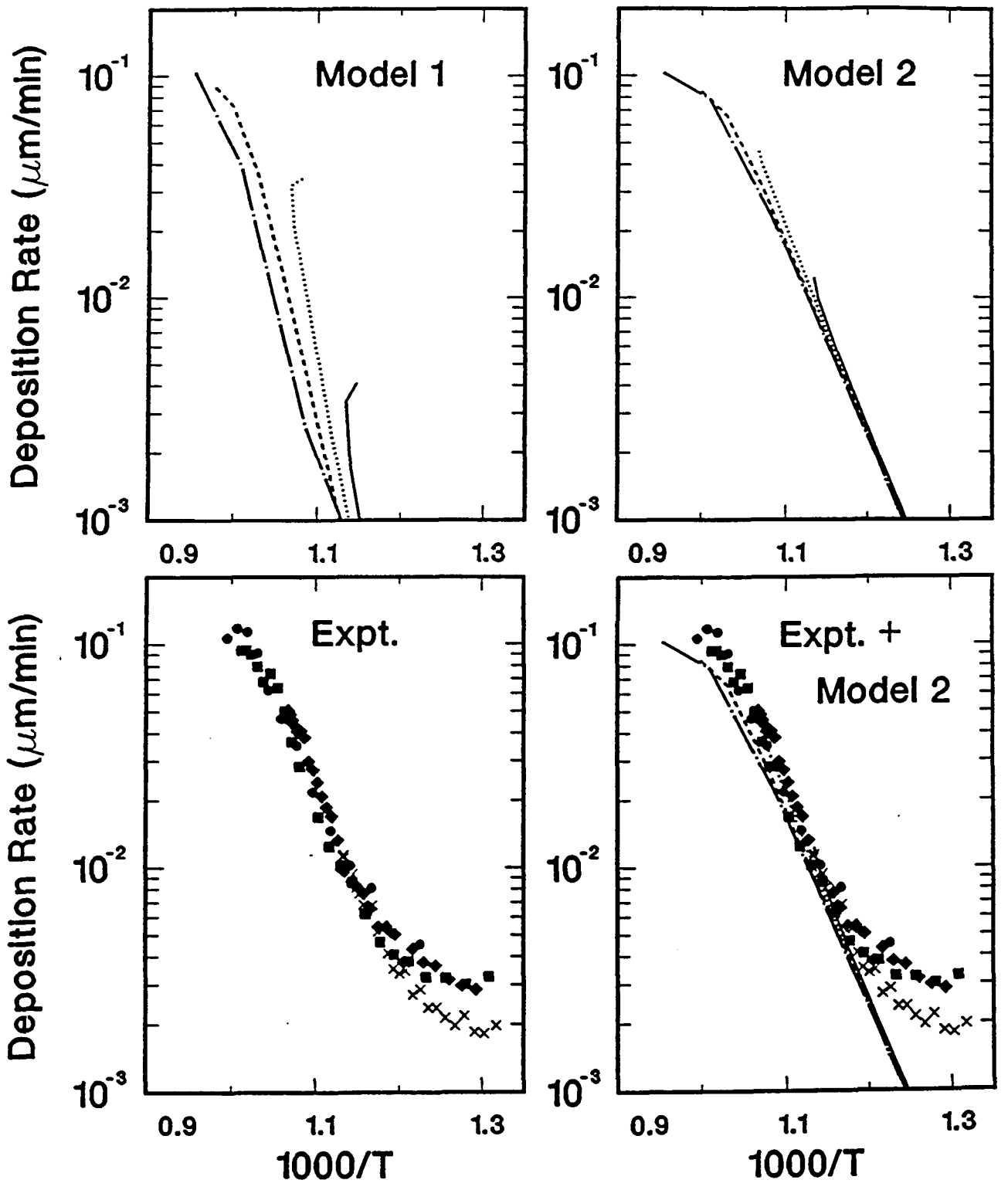
Model 1
Model 2
Expt.
Expt. +
Model 2
Deposition Rate (μm/min)
Deposition Rate (μm/min)
10^-1
10^-2
10^-3
0.9
1.1
1.3
1000/T
1000/T

Fig. 7

UNLIMITED DISTRIBUTION

INITIAL DISTRIBUTION

Massachusetts Institute of Technology
Attn: K. F. Jensen
Chemical Engineering Department
Cambridge, MA 02139

Sematech
Attn: F. T. Geyling
2706 Montopolis Drive
Austin, TX 78741

University of Houston
Attn: R. Pollard
Department of Chemical Engineering
Houston, TX 77004

1120 J. B. Gerardo
1126 A. W. Johnson
1126 W. G. Breiland (50)
1126 M. E. Coltrin (10)
1126 P. Ho
8245 R. J. Kee
8245 G. H. Evans
8245 F. M. Rupley
3141 S. A. Landenberger (5)
3141-1 C. L. Ward(8) for DOE/OSTI
3151 W. I. Klein(3)
8524 J. A. Wackerly